

Structure and superconductivity in the binary  $\text{Re}_{1-x}\text{Mo}_x$  alloysT. Shang,<sup>1,2,3,\*</sup> D. J. Gawryluk,<sup>1,†</sup> J. A. T. Verezhak,<sup>4</sup> E. Pomjakushina,<sup>1</sup> M. Shi,<sup>2</sup> M. Medarde,<sup>1</sup> J. Mesot,<sup>5,3,6</sup> and T. Shiroka<sup>6,5,‡</sup><sup>1</sup>Laboratory for Multiscale Materials Experiments, Paul Scherrer Institut, Villigen CH-5232, Switzerland<sup>2</sup>Swiss Light Source, Paul Scherrer Institut, Villigen CH-5232, Switzerland<sup>3</sup>Institute of Condensed Matter Physics, École Polytechnique Fédérale de Lausanne (EPFL), Lausanne CH-1015, Switzerland<sup>4</sup>Laboratory for Muon-Spin Spectroscopy, Paul Scherrer Institut, CH-5232 Villigen PSI, Switzerland<sup>5</sup>Paul Scherrer Institut, CH-5232 Villigen PSI, Switzerland<sup>6</sup>Laboratorium für Festkörperphysik, ETH Zürich, CH-8093 Zurich, Switzerland

(Received 15 November 2018; revised manuscript received 7 January 2019; published 7 February 2019)

The binary  $\text{Re}_{1-x}\text{Mo}_x$  alloys, known to cover the full range of solid solutions, were successfully synthesized and their crystal structures and physical properties investigated via powder x-ray diffraction, electrical resistivity, magnetic susceptibility, and heat capacity. By varying the Re/Mo ratio, we explore the full  $\text{Re}_{1-x}\text{Mo}_x$  binary phase diagram, in all its four different solid phases: hcp-Mg ( $P6_3/mmc$ ),  $\alpha$ -Mn ( $I\bar{4}3m$ ),  $\beta$ -CrFe ( $P4_2/mnm$ ), and bcc-W ( $Im\bar{3}m$ ), of which the second is noncentrosymmetric with the rest being centrosymmetric. All  $\text{Re}_{1-x}\text{Mo}_x$  alloys are superconductors, whose critical temperatures exhibit a peculiar phase diagram, characterized by three different superconducting regions. In most alloys, the  $T_c$  is almost an order of magnitude higher than in pure Re and Mo. Low-temperature electronic specific-heat data evidence a fully gapped superconducting state, whose enhanced gap magnitude and specific-heat discontinuity suggest a moderately strong electron-phonon coupling across the series. Considering that several  $\alpha$ -Mn-type  $\text{Re}T$  alloys ( $T$  = transition metal) show time-reversal symmetry breaking (TRSB) in the superconducting state, while TRS is preserved in the isostructural  $\text{Mg}_{10}\text{Ir}_{19}\text{B}_{16}$  or  $\text{Nb}_{0.5}\text{Os}_{0.5}$ , the  $\text{Re}_{1-x}\text{Mo}_x$  alloys represent another suitable system for studying the interplay of space-inversion, gauge, and time-reversal symmetries in future experiments expected to probe TRSB in the  $\text{Re}T$  family.

DOI: 10.1103/PhysRevMaterials.3.024801

## I. INTRODUCTION

Time reversal and spatial inversion are two key symmetries, which radically influence electron pairing in the superconducting state. Superconductors with a space-inversion center can host either even-parity spin-singlet (e.g.,  $s$ - or  $d$ -wave) or odd-parity spin-triplet (e.g.,  $p$ -wave) pairing states. These strict symmetry requirements, however, are relaxed in noncentrosymmetric superconductors (NCSCs), where the antisymmetric spin-orbit coupling (ASOC) allows, in principle, the occurrence of parity-mixed superconducting states, whose mixing degree is related to the strength of the ASOC and to other microscopic parameters [1,2]. Because of the mixed pairing, NCSCs frequently display interesting properties. For instance, some NCSCs, such as  $\text{CePt}_3\text{Si}$  [3],  $\text{CeIrSi}_3$  [4],  $\text{Li}_2\text{Pt}_3\text{B}$  [5,6],  $\text{K}_2\text{Cr}_3\text{As}_3$  [7,8], and  $\text{YBiPt}$  [9] exhibit line nodes in the gap, while others, such as  $\text{LaNiC}_2$  [10] and  $(\text{La,Y})_2\text{C}_3$  [11], show multiple-gap superconductivity. The external pressure drives  $\text{CeIrSi}_3$  into a gapless superconductor [12], while a nodal behavior has been observed in  $\text{LaNiC}_2$  and  $\text{Y}_2\text{C}_3$  [13–15]. Recently, many NCSCs [2,9,16,16–21], in particular  $\text{YPtBi}$  [9],  $\text{BiPd}$  [20], and  $\text{PbTaSe}_2$  [21], have

been closely investigated as possible models of topological superconductors.

Interestingly, numerous muon-spin relaxation/rotation ( $\mu\text{SR}$ ) studies have revealed that some NCSCs exhibit also time-reversal symmetry breaking (TRSB), concomitant with the onset of superconductivity. Examples include  $\text{LaNiC}_2$  [22],  $\text{La}_7(\text{Ir,Rh})_3$  [23,24], and several Re-based binary alloys  $\text{Re}T$  ( $T$  = transition metal, e.g., Ti, Zr, Nb, Hf) [25–29]. In general, the breaking of time-reversal symmetry below  $T_c$  and a lack of space-inversion symmetry of the crystal structure are independent events, not required to occur together. For instance, TRS is broken in several  $\alpha$ -Mn-type  $\text{Re}T$  compounds and in the pure elementary Re [29], yet it is preserved in the isostructural  $\text{Mg}_{10}\text{Ir}_{19}\text{B}_{16}$  or  $\text{Nb}_{0.5}\text{Os}_{0.5}$  [30,31], clearly suggesting that TRSB is most likely related to the presence of Re atoms, rather than to a generic lack of space-inversion symmetry. Indeed, by converse, the centrosymmetric  $\text{Sr}_2\text{RuO}_4$ ,  $\text{PrOs}_4\text{Ge}_{12}$ , and  $\text{LaNiGa}_2$  also exhibit a broken TRS in the superconducting state [32–34].

To further study the TRSB in  $\text{Re}T$  materials, one should identify a system that exhibits both centro- and noncentrosymmetric structures, while still preserving its basic stoichiometry. For instance, depending on synthesis protocol,  $\text{Re}_3\text{W}$  can be either a centro- (hcp-Mg-type) or a noncentrosymmetric ( $\alpha$ -Mn-type) superconductor [35], yet neither is found to break TRS [36]. On the other hand, other superconducting  $\text{Re}T$  compounds, with  $T$  = Ti, Zr, Nb, Hf, indeed, break TRS, yet mostly adopt the same ( $\alpha$ -Mn-type) structure. Similar to the  $\text{Re}_3\text{W}$  case, the  $\text{Re}_{1-x}\text{Mo}_x$  binary alloys discussed

\*Corresponding author: tian.shang@psi.ch

†Corresponding author: dariusz.gawryluk@psi.ch; On leave from Institute of Physics, Polish Academy of Sciences, Aleja Lotników 32/46, PL-02-668 Warsaw, Poland.

‡Corresponding author: tshiroka@phys.ethz.ch

here represent another candidate system. For different Re/Mo ratios, depending on synthesis protocol, they adopt either centro- or noncentrosymmetric structures [37]. Although the superconductivity of several  $\text{Re}_{1-x}\text{Mo}_x$  alloys was reported decades ago, only recently the Mo-rich side was studied by different techniques [38–41]. To date, a systematic study of the full range of  $\text{Re}_{1-x}\text{Mo}_x$  solid solution is missing. In particular, due to synthesis difficulties, its Re-rich side remains largely unexplored. Yet, in view of the noncentrosymmetric structures adopted, it is precisely this part of the phase diagram to be the most interesting one.

In this paper, based on systematic physical-property measurements, we explore the full superconducting phase diagram of the  $\text{Re}_{1-x}\text{Mo}_x$  system. To this aim, polycrystalline  $\text{Re}_{1-x}\text{Mo}_x$  samples, with  $0.12 \leq x \leq 0.75$ , were successfully synthesized. Although samples with different Re/Mo ratios exhibit different crystal structures, they all become superconductors (whose highest  $T_c$  reaches 12.4 K). All the relevant superconducting parameters, including gap values and symmetries, were determined by magnetometry, transport, and specific-heat measurements, thus allowing us to present the complete  $\text{Re}_{1-x}\text{Mo}_x$  superconducting phase diagram.

After briefly describing the experimental methods in Sec. II, we present the key results in Sec. III, including those of chemical composition, crystal structure, electrical resistivity, magnetization, and specific heat. Finally, the overall superconducting phase diagram is presented and discussed in Sec. IV.

## II. EXPERIMENTAL DETAILS

Polycrystalline  $\text{Re}_{1-x}\text{Mo}_x$  ( $0.12 \leq x \leq 0.75$ ) alloys were prepared by arc melting Re and Mo metals with different stoichiometric ratios in high-purity argon atmosphere. To improve the homogeneity, samples were flipped and remelted several times and, for some of them, the as-cast ingots were annealed at 900 °C for two weeks. The  $\beta$ -CrFe phase (e.g.,  $\text{Re}_{0.6}\text{Mo}_{0.4}$ ) was obtained by interrupting the heating immediately after the melting of the precursors. Hence, all the measurements reported here for the  $\beta$ -CrFe phase refer to as-cast samples. The extra phases were obtained by further annealing the as-cast samples. The  $\alpha$ -Mn phase with a noncentrosymmetric crystal structure ( $\text{Re}_{0.77}\text{Mo}_{0.23}$ ) was stabilized by annealing the sample over one week at 1400 °C in argon or hydrogen atmosphere. Unlike the rather malleable Mo-rich alloys, their Re-rich counterparts turned out to be extremely hard. In addition, the  $\text{Re}_{0.77}\text{Mo}_{0.23}$  alloy resulted fragile after annealing at 1400 °C. Previously, the same arc-melting processes were adopted to cover the whole  $x$  range [42,43], with the samples being annealed at 1200 °C and then quenched in water. However, these early attempts failed to produce clean  $\alpha$ -Mn phase.

The x-ray powder diffraction (XRD) patterns were measured at room temperature by using a Bruker D8 diffractometer with Cu  $K_\alpha$  radiation. The atomic ratios of the  $\text{Re}_{1-x}\text{Mo}_x$  samples were measured by x-ray fluorescence spectroscopy (XRF) on an AMETEK Orbis Micro-XRF analyzer. The magnetic susceptibility, electrical resistivity, and specific-heat measurements were performed on a 7-T Quantum Design Magnetic Property Measurement System (MPMS-7) and a 9-T Physical Property Measurement System (PPMS-9).

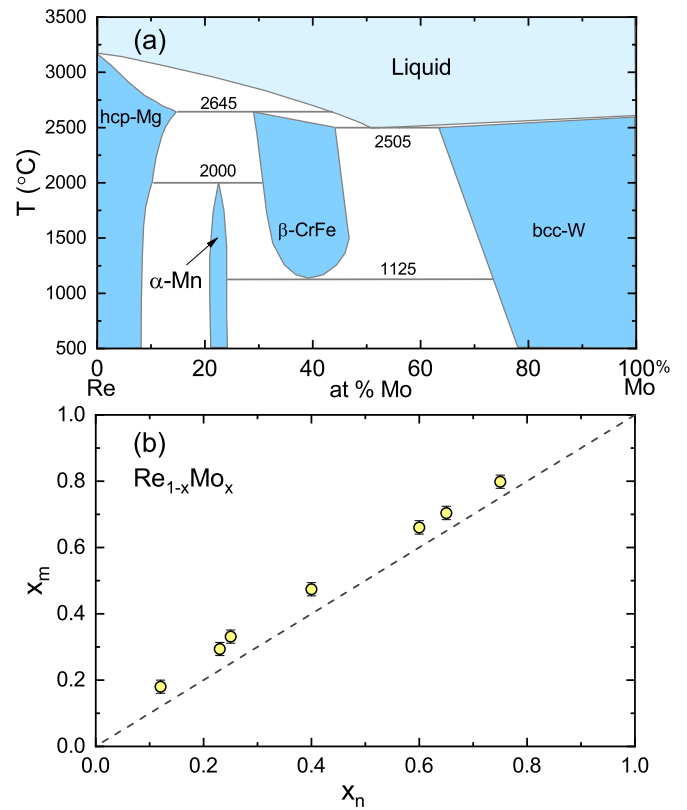
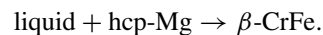
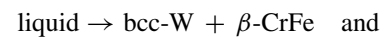


FIG. 1. (a) Binary phase diagram of  $\text{Re}_{1-x}\text{Mo}_x$  alloys (data adapted from Ref. [37]). In our case, more than ten samples with different Re/Mo ratios were synthesized. (b) Measured Mo concentration  $x_m$  vs the nominal  $x_n$  value. The dashed-line refers to the ideal case where the two values coincide.

## III. KEY EXPERIMENTAL RESULTS

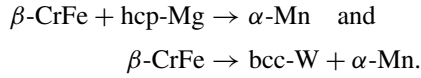
### A. Crystal structures

As shown in Fig. 1(a), the  $\text{Re}_{1-x}\text{Mo}_x$  binary alloys exhibit a very rich phase diagram. While pure Mo and Re form body-centered-cubic (bcc) and hexagonal-close-packed (hcp) structures, respectively, at intermediate Re/Mo ratios two other phases appear, a tetragonal  $\beta$ -CrFe and a cubic  $\alpha$ -Mn phase. By suitably combining arc melting and annealing processes, we could successfully synthesize pure-phase alloys representative of all four crystal structures. Although the  $\text{Re}_{1-x}\text{Mo}_x$  phase diagram has been studied before, most of the obtained samples contained at least two different solid phases, thus preventing a systematic study of their physical properties [42,43]. Conforming to the binary phase diagram, the bcc-W and hcp-Mg solid phases were easily obtained via arc melting of Re and Mo and resulted to be stable at 1400 °C. Two reactions take place during the solidifying process:



In order to synthesize the pure  $\beta$ -CrFe phase, the first reaction was blocked by interrupting the heating immediately after the melting of both the Re and Mo metals. As for the  $\alpha$ -Mn phase, this cannot be synthesized via arc melting, since no such phase appears during the liquid-mixture cooling. Yet,

two other reactions include this phase



Since in both cases solid-state reactions are involved, the pure  $\alpha$ -Mn phase was obtained by annealing the melted Re and Mo metals at 1400 °C.

Subsequently, the Re/Mo atomic ratio was determined via Micro-XRF on polished samples. The estimated Mo (or Re) concentration versus its nominal value is presented in Fig. 1(b). For all the samples, the measured Re (Mo) concentration was slightly smaller (larger) than the nominal value, reflecting the preferential evaporation of Re during the arc melting process. For clarity, since typical deviations do not exceed  $\approx 12\%$ , the nominal concentrations will be used hereafter.

Figure 2 shows four representative XRD patterns of polycrystalline  $\text{Re}_{1-x}\text{Mo}_x$  samples, with the other samples exhibiting similar diffractograms (not shown here). All the XRD patterns were analyzed using the FULLPROF Rietveld-analysis suite [44]. No obvious impurity phases could be detected, indicating the high quality of the synthesized samples. As shown in Fig. 1(a), on the Re-rich side,  $\text{Re}_{1-x}\text{Mo}_x$  alloys adopt a hexagonal hcp-Mg-type structure. According to our XRD refinements in Fig. 2(a), all the samples with  $0.12 \leq x \leq 0.25$  exhibit hcp-Mg-type structures [see inset in Fig. 2(a)]. Following the binary phase diagram, for  $x = 0.23$  besides the hexagonal structure, a cubic  $\alpha$ -Mn-type structure can also be stabilized by sample annealing at 1400 °C [see Fig. 2(b)]. Such cubic phase is the same as that adopted by other  $\text{ReT}$  compounds, where TRSB and unconventional superconductivity have been frequently observed (see Sec. I). However, unlike in other  $\text{ReT}$  binary alloys, in  $\text{Re}_{1-x}\text{Mo}_x$  the  $\alpha$ -Mn-type phase region is extremely narrow [see Fig. 1(a)], i.e.,  $0.21 \leq x \leq 0.25$ . To exclude the hcp-Mg phase, the Re concentration was kept fixed at  $(1-x) = 0.77$ , i.e., at the center of the  $\alpha$ -Mn-phase region. By further increasing Mo concentration, the tetragonal  $\beta$ -CrFe-type solid phase was synthesized via quenching. Its XRD refinement and crystal structure are presented in Fig. 2(c). There are five different Re sites in the unit cell. Further on, in the Mo-rich side, the  $\text{Re}_{1-x}\text{Mo}_x$  alloys adopt a cubic bcc-W-type crystal structure. As an example, in Fig. 2(d) we show the XRD refinement of the  $x = 0.4$  sample, along with its crystal structure (see inset). The crystal-structure information and atomic coordinates for all the four different solid phases are reported in Tables I and II, respectively.

### B. Electrical resistivity

The temperature-dependent electrical resistivity  $\rho(T)$  of  $\text{Re}_{1-x}\text{Mo}_x$  ( $0.12 \leq x \leq 0.75$ ) was measured from room temperature down to 2 K. As shown in Fig. 3(a), all samples exhibit metallic behavior down to the lowest temperature. Apart from the superconducting transition, no anomaly associated with structural, magnetic, or charge-density-wave transitions could be detected. The room-temperature (295 K) electrical resistivities versus Mo concentration  $x$  are summarized in Fig. 4. Upon increasing Mo content, the electrical resistivity also increases, before reaching the first phase boundary be-

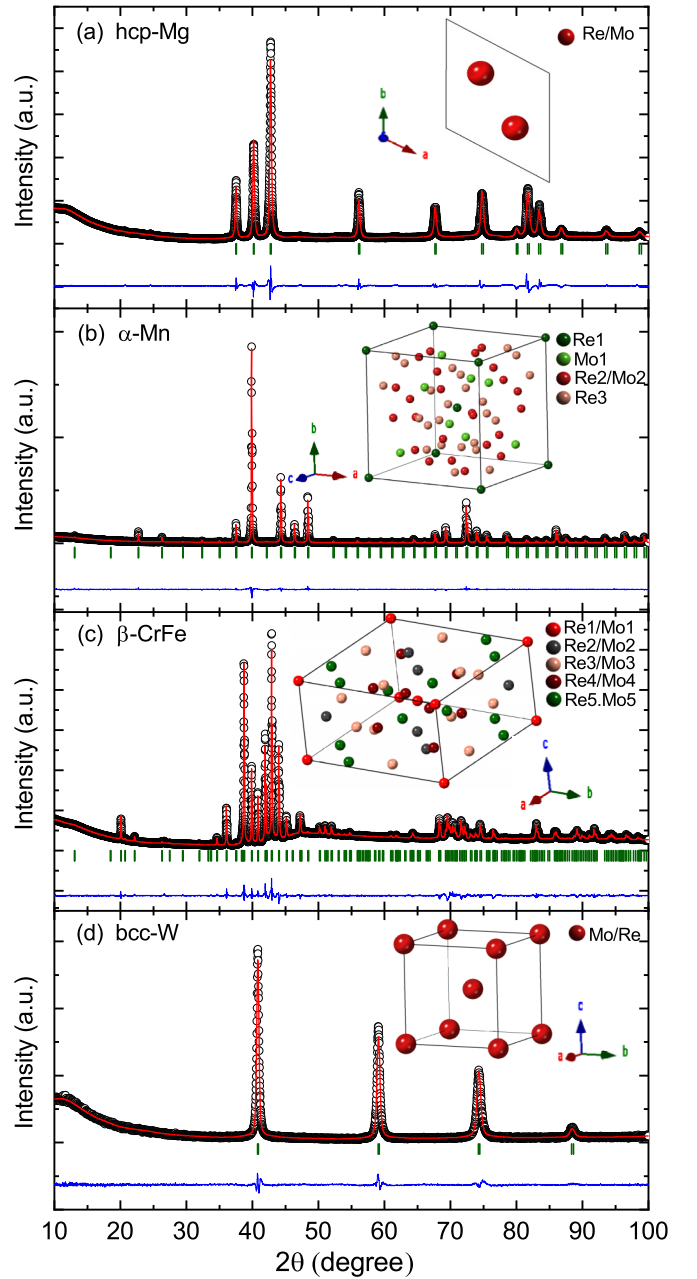


FIG. 2. Room-temperature XRD patterns and refinements for  $\text{Re}_{0.88}\text{Mo}_{0.12}$  (a),  $\text{Re}_{0.77}\text{Mo}_{0.23}$  (b),  $\text{Re}_{0.6}\text{Mo}_{0.4}$  (c), and  $\text{Re}_{0.4}\text{Mo}_{0.6}$  (d). The black open circles and the solid red lines represent experimental patterns and Rietveld-refinement profiles, respectively. The blue lines show the residuals, i.e., the difference between calculated and experimental data. The vertical green bars mark the calculated Bragg-peak positions. In each case, the (unit-cell) crystal structures are shown in the insets.

tween hcp-Mg and  $\beta$ -CrFe phases. We note that, for  $x = 0.23$ , a noncentrosymmetric  $\alpha$ -Mn-type sample (shown by a star in Fig. 4) exhibits a 25% larger electrical resistivity compared to its centrosymmetric hcp-Mg-type counterpart. As  $x$  is further increased beyond 0.3, the  $\text{Re}_{1-x}\text{Mo}_x$  alloys adopt the  $\beta$ -CrFe phase and the electrical resistivity starts to decrease. On the Mo-rich side, i.e., in the bcc-W phase, electrical resistivity is much smaller than on the Re-rich side, thus demonstrating the

TABLE I. Crystal structure, space group, and refined lattice parameters for four representative phases of the  $\text{Re}_{1-x}\text{Mo}_x$  binary alloy, with Mo concentrations  $x = 0.12, 0.23, 0.4$ , and  $0.6$ .

Sample	$\text{Re}_{0.88}\text{Mo}_{0.12}$	$\text{Re}_{0.77}\text{Mo}_{0.23}$	$\text{Re}_{0.6}\text{Mo}_{0.4}$	$\text{Re}_{0.4}\text{Mo}_{0.6}$
Structure	hexagonal hcp-Mg	cubic $\alpha$ -Mn	tetragonal $\beta$ -CrFe	cubic bcc-W
Space group	$P6_3/mmc$ (No. 194)	$I\bar{4}3m$ (No. 217)	$P4_2/mnm$ (No. 136)	$Im\bar{3}m$ (No. 229)
$a$ (Å)	2.76798(2)	9.58476(3)	9.58514(4)	3.12627(10)
$b$ (Å)	2.76798(2)	9.58476(3)	9.58514(4)	3.12627(10)
$c$ (Å)	4.48728(5)	9.58476(3)	4.97891(2)	3.12627(10)
$V_{\text{cell}}$ (Å <sup>3</sup> )	29.7743(5)	880.529(6)	457.437(4)	30.5549(17)

better metallicity of this phase. Overall, these results clearly indicate a close relationship between the crystal structure and the electronic properties in the binary  $\text{Re}_{1-x}\text{Mo}_x$  alloys.

The electrical resistivity in the low-temperature region is plotted in Fig. 3(b). Despite the varying  $T_c$ s across the  $\text{Re}_{1-x}\text{Mo}_x$  series, all the samples exhibit a superconducting transition at low temperature. The  $T_c$  values vary nonmonotonically with Re (or Mo) concentration, with the maximum  $T_c = 13$  K being achieved for  $x = 0.6$ .  $T_c$  values resulting from electrical-resistivity data are summarized in Fig. 7 (see below). Finally, the centrosymmetric  $x = 0.23$  specimen shows a  $\sim 1$  K higher  $T_c$  than the noncentrosymmetric one.

### C. Magnetic susceptibility

The bulk superconductivity of  $\text{Re}_{1-x}\text{Mo}_x$  alloys was further confirmed by magnetic susceptibility measurements. The temperature dependence of the magnetic susceptibility  $\chi(T)$

was measured using both field-cooled (FC) and zero-field-cooled (ZFC) protocols in an applied field of 1 mT. As shown in Fig. 5(a) and 5(b), all the samples show superconducting transitions with different  $T_c$ s, consistent with the respective values determined from electrical resistivity (see Fig. 3). The splitting of the FC- and ZFC-susceptibilities is a typical feature of type-II superconductors, where the magnetic-field flux is pinned once the material is cooled in an applied field. Since  $\chi_v^{\text{SI}} \sim 1$ , the ZFC susceptibility data indicate (almost ideal) bulk superconductivity below  $T_c$ .

### D. Specific heat

In the superconducting state, specific-heat data offer valuable insight into the superconducting properties, including the gap value and its symmetry. Hence, in the  $\text{Re}_{1-x}\text{Mo}_x$  series, we performed systematic zero-field specific-heat measurements down to 2 K. As shown in Fig. 6, in all cases

TABLE II. Refined atomic coordinates and site occupancy factor (SOF) of four different crystal structures of  $\text{Re}_{1-x}\text{Mo}_x$  alloys with  $x = 0.12, 0.23, 0.4$ , and  $0.6$ .

Atom	Wyckoff	$x$	$y$	$z$	SOF
<b><math>\text{Re}_{0.88}\text{Mo}_{0.12}</math></b>					
Re1	2c	0.33330	0.66670	0.25000	0.88
Mo1	2c	0.33330	0.66670	0.25000	0.12
<b><math>\text{Re}_{0.77}\text{Mo}_{0.23}</math></b>					
Mo1	8c	0.3260(4)	0.3260(4)	0.3260(4)	1
Mo2	24g	0.3593(2)	0.3593(2)	0.0409(3)	0.30(1)
Re1	2a	0	0	0	1
Re2	24g	0.3593(2)	0.3593(2)	0.0409(3)	0.70(1)
Re3	24g	0.0911(2)	0.0911(2)	0.2839(2)	1
<b><math>\text{Re}_{0.6}\text{Mo}_{0.4}</math></b>					
Re1	2a	0	0	0	0.69(1)
Re2	4f	0.3994(2)	0.3994(2)	0	0.22(1)
Re3	8i	0.4650(1)	0.1303(2)	0	0.52(1)
Re4	8i	0.7418(2)	0.0655(2)	0	0.75(1)
Re5	8j	0.1834(1)	0.1834(2)	0.25	0.60(1)
Mo1	2a	0	0	0	0.31(1)
Mo2	4f	0.3994(2)	0.3994(2)	0	0.78(1)
Mo3	8i	0.4650(1)	0.1303(2)	0	0.48(1)
Mo4	8i	0.7418(2)	0.0655(2)	0	0.25(1)
Mo5	8j	0.1834(1)	0.1834(2)	0.25	0.40(1)
<b><math>\text{Re}_{0.4}\text{Mo}_{0.6}</math></b>					
Re1	2a	0	0	0	0.4
Mo1	2a	0	0	0	0.6



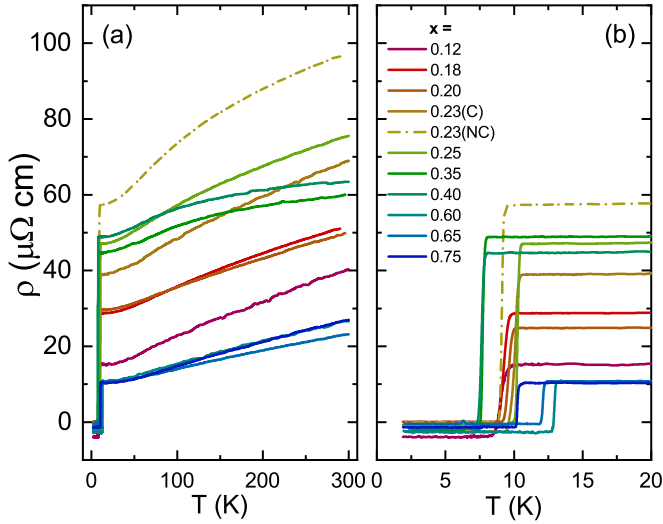


FIG. 3. (a) Temperature dependence of the electrical resistivity of  $\text{Re}_{1-x}\text{Mo}_x$  ( $0.12 \leq x \leq 0.75$ ). (b) Enlarged low-temperature data region, highlighting the superconducting transitions. For  $x = 0.23$ , the electrical resistivity of both centro- (C) and noncentrosymmetric (NC) specimens (dashed-dotted line) are shown.

a clear specific-heat jump indicates a bulk superconducting transition. Again, the  $T_c$  values determined by using the equal-entropy method are summarized in the superconducting phase diagram below. The electronic specific heat  $C_e/T$  was obtained by subtracting the phonon contribution from the experimental data. An example is shown in the inset of Fig. 6, where the normal-state heat capacity of  $\text{Re}_{0.77}\text{Mo}_{0.23}$  (NC) is fitted to  $C = \gamma_n T + \beta T^3 + \delta T^5$ , where  $\gamma_n T$  is the normal-state-electronic contribution to heat capacity and  $\beta T^3 + \delta T^5$  is the phonon contribution to heat capacity. The specific heat of all the samples was fitted using the same formula and the derived  $\beta$  and  $\delta$  values (as listed in Table III) were then used to account for the phonon contribution in the superconducting

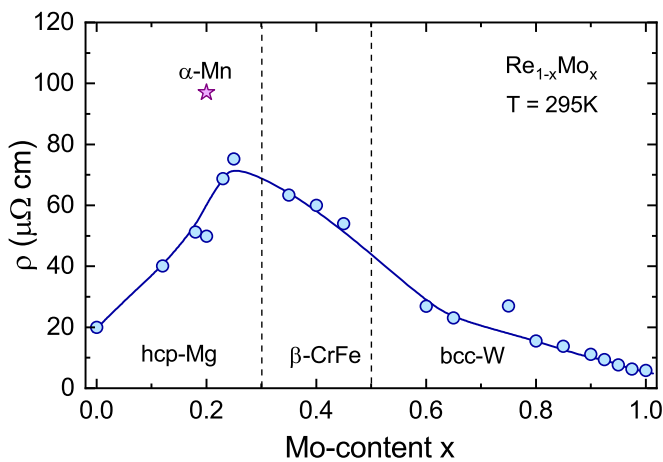


FIG. 4. Room-temperature electrical resistivity of  $\text{Re}_{1-x}\text{Mo}_x$  vs Mo concentration  $x$ . The star represents the resistivity of  $\text{Re}_{0.77}\text{Mo}_{0.23}$  with noncentrosymmetric  $\alpha$ -Mn-type structure, here 25% higher than that of its centrosymmetric hcp-Mg counterpart. The dashed lines indicate the solid-phase boundaries. Data for pure Re and  $\text{Re}_{1-x}\text{Mo}_x$  ( $0.8 \leq x \leq 1$ ) were taken from Refs. [45–47].

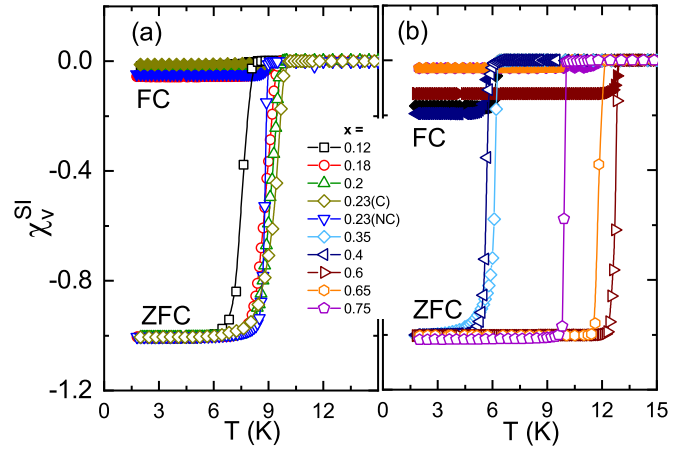


FIG. 5. Temperature dependence of the magnetic susceptibility  $\chi(T)$  of  $\text{Re}_{1-x}\text{Mo}_x$  ( $0.12 \leq x \leq 0.75$ ). Data were collected in an applied field of 1 mT and a temperature range of 1.8 to 15 K. The magnetic susceptibilities were corrected by using the demagnetization factors obtained from the field-dependent magnetization at base temperature.

state. The extrapolation to a zero intercept of the  $C/T$  data close to 0 K (in the inset of Fig. 6) indicates a fully superconducting volume fraction and a good sample quality. The Debye temperature  $\Theta_D$  can be calculated from  $\beta$  values, by using  $\Theta_D = (12\pi^4 R n / 5\beta)^{1/3}$ , where  $R = 8.314 \text{ J K}^{-1} \text{ mol}^{-1}$  is the molar gas constant and  $n = 1$  is the number of atoms per formula unit. The  $\gamma_n$  and  $\Theta_D$  values of  $\text{Re}_{1-x}\text{Mo}_x$  alloys are summarized in Table III. The density of states (DOS) at the Fermi level  $N(\epsilon_F)$  was evaluated from the expression  $N(\epsilon_F) = \pi^2 k_B^2 / 3\gamma_n$ , where  $k_B$  and  $\gamma_n$  are the Boltzmann constant and the normal-state electronic-specific-heat coefficient [52]. The electron-phonon coupling constant  $\lambda_{ep}$ , a measure of the attractive interaction between electrons and phonons, can be further estimated from the  $\Theta_D$  and  $T_c$  values by applying

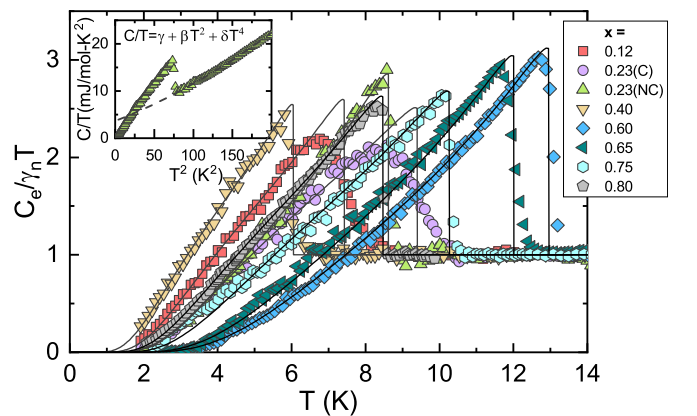


FIG. 6. Temperature dependence of the normalized electronic specific heat  $C_e/\gamma_n T$  for  $\text{Re}_{1-x}\text{Mo}_x$  with  $x = 0.12, 0.20, 0.23$  (C and NC), 0.40, 0.6, 0.75, and 0.80. (Inset) Specific heat  $C/T$  as a function of  $T^2$  for the noncentrosymmetric  $\text{Re}_{0.77}\text{Mo}_{0.23}$ . The dashed line in the inset is a fit to  $C/T = \gamma + \beta T^2 + \delta T^4$ , while the solid lines in the main panel are fits to a fully gapped  $s$ -wave model. Data for  $x = 0.80$  were taken from Ref. [47].

TABLE III. Superconducting transition temperatures  $T_c$ , specific-heat fit parameters, estimated Debye temperatures, density of states, and electron-phonon coupling constants for the  $\text{Re}_{1-x}\text{Mo}_x$  series.

$x$	$T_c^{Cp}$ (K)	$\gamma_n$ (mJ mol <sup>-1</sup> K <sup>-2</sup> )	$\Theta_D$ (K)	$\Delta C/(\gamma_n T_c)$	$\Delta/(k_B T_c)$	$\lambda_{ep}$	$N(\epsilon_F)$ (eV f.u.)	$N_{\text{band}}(\epsilon_F)$ (eV f.u.)	$m^*/m_e$
0.00 <sup>a</sup>	1.69	2.30	415.0	1.30	1.71	0.46	0.33	0.27	1.46
0.12	7.45	3.80	402.9	1.18	1.85	0.66	1.61	0.97	1.66
0.20	9.02	3.77	363.7	0.98	1.80	0.72	1.60	0.93	1.72
0.23 <sup>b</sup>	9.43	3.53	333.0	1.07	1.80	0.77	1.50	0.85	1.77
0.23 <sup>c</sup>	8.65	3.66	311.4	1.90	2.00	0.76	1.55	0.88	1.76
0.35	6.30	3.20	391.1	1.51	1.90	0.63	1.36	0.83	1.63
0.40	6.07	3.01	520.0	1.44	1.82	0.58	1.28	0.81	1.58
0.45	6.60	3.45	397.2	1.59	1.85	0.64	1.46	0.89	1.64
0.60	13.00	4.05	341.8	2.00	2.14	0.87	1.72	0.92	1.87
0.65	12.05	3.89	397.3	1.96	2.10	0.79	1.65	0.92	1.79
0.75	10.30	3.69	480.6	1.64	1.90	0.69	1.57	0.93	1.69
0.80 <sup>a</sup>	8.50	3.65	420.7	1.51	1.87	0.68	1.55	0.92	1.68
0.85 <sup>a</sup>	6.74	3.41	436.2	1.50	1.85	0.62	1.45	0.89	1.62
0.90 <sup>a</sup>	3.02	2.39	429.9	1.35	1.80	0.51	1.01	0.66	1.51
1.00 <sup>a</sup>	0.92	1.83	460.0	1.25	1.70	0.41	0.28	0.20	1.41

<sup>a</sup>Data from Refs. [47–51].<sup>b</sup>Centrosymmetric.<sup>c</sup>Noncentrosymmetric.

the semi-empirical McMillan formula [53]:

$$\lambda_{ep} = \frac{1.04 + \mu^* \ln(\Theta_D/1.45 T_c)}{(1 - 0.62 \mu^*) \ln(\Theta_D/1.45 T_c) - 1.04}. \quad (1)$$

The Coulomb pseudopotential  $\mu^*$ , usually lying in the 0.09–0.18 range, is here fixed to 0.13, a commonly used value for the transition metals. As listed in Table III, the enhanced electron-phonon coupling  $\lambda_{ep}$  of  $\text{Re}_{1-x}\text{Mo}_x$  (compared with pure Re or Mo) implies a moderate coupling strength of electrons in the superconducting state. Similar  $\lambda_{ep}$  values have been found also in other noncentrosymmetric ReT compounds [54–57]. Finally, the band-structure density of states (DOS)  $N_{\text{band}}(\epsilon_F)$  and the effective mass of quasiparticles  $m^*$  can be estimated from the relations  $N_{\text{band}}(\epsilon_F) = N(\epsilon_F)/(1 + \lambda_{ep})$  and  $m^* = m_{\text{band}}(1 + \lambda_{ep})$  [52]. Here we assume  $m_{\text{band}} = m_e$ , where  $m_e$  is the mass of free electrons. The calculated values for the  $\text{Re}_{1-x}\text{Mo}_x$  alloys are summarized in Table III. For the noncentrosymmetric  $\text{Re}_{0.77}\text{Mo}_{0.23}$ , the DOS is comparable to the values resulting from band-structure calculations on the similar ReT ( $T = \text{Zr, Nb, Ti}$ ) compounds [56,58].

Below we discuss the  $\text{Re}_{1-x}\text{Mo}_x$  superconducting properties based on specific-heat data. The derived electronic specific heats divided by the normal-state electronic specific-heat coefficients, i.e.,  $C_e/\gamma_n T$ , are shown in the main panel of Fig. 6 as a function of temperature. The temperature-dependent superconducting-phase contribution to the entropy can be calculated by using the following equation:

$$S = \frac{6\gamma_n}{\pi^2} \frac{\Delta(0)}{k_B} \int_0^\infty [f \ln f + (1-f) \ln(1-f)] dx, \quad (2)$$

where  $f = (1 + e^{E/k_B T})^{-1}$  is the Fermi function,  $\Delta(0)$  is the SC gap value at 0 K, and  $E(\epsilon) = \sqrt{\epsilon^2 + \Delta^2(T)}$  is the excitation energy of quasiparticles (i.e., their dispersion), with  $\epsilon$  the electron energies measured relative to the chemical potential (Fermi energy) [59,60]. Here  $\Delta(T) = \Delta(0) \tanh\{1.82[1.018(T_c/T - 1)]^{0.51}\}$  [61]. Once the entropy

is known, the temperature-dependent electronic specific heat in the superconducting state can be calculated from  $C_e = T \frac{dS}{dT}$ . The solid lines in Fig. 6 represent fits with the above model and a single isotropic gap. The derived superconducting gap values  $\Delta/(k_B T_c)$  are summarized in Table III. Except for the pure Re or Mo, the gap values of  $\text{Re}_{1-x}\text{Mo}_x$  alloys are slightly higher than the weak-coupling BCS value 1.763, thus indicating moderately coupled superconducting pairs in  $\text{Re}_{1-x}\text{Mo}_x$ . The specific-heat discontinuities at  $T_c$ , i.e.,  $\Delta C/\gamma_n T_c$ , are also summarized in Table III. As shown in Fig. 6,  $\text{Re}_{1-x}\text{Mo}_x$  alloys with  $x = 0.23$  (NC), 0.40, 0.60, and 0.75, show a larger specific-heat discontinuity than the conventional BCS value of 1.43, whereas for  $x = 0.12, 0.20$ , and 0.23(C), the analogous discontinuity is reduced, most likely reflecting a broadening of the superconducting transition.

#### IV. PHASE DIAGRAM AND DISCUSSION

Based on the above experimental data, in Fig. 7, we present the superconducting phase diagram of the  $\text{Re}_{1-x}\text{Mo}_x$  alloys as a function of the Re/Mo concentration. According to the binary phase diagram (Fig. 1) and to XRD refinements (Fig. 2), a change in the relative Re/Mo content induces up to four different solid phases: hcp-Mg ( $P6_3/mmc$ ),  $\alpha$ -Mn ( $I\bar{4}3m$ ),  $\beta$ -CrFe ( $P4_2/mnm$ ), and bcc-W ( $Im\bar{3}m$ ).

As the Mo concentration increases, the  $T_c$  varies nonmonotonically, giving rise to three distinct superconducting regions (see Fig. 7). The first superconducting region, with highest  $T_c = 9.43$  K, is achieved on the Re-rich part for  $x = 0.23$  and corresponds to samples adopting an hcp-Mg-type structure. Note that this  $T_c$  is  $\approx 1$  K higher than that of the corresponding  $\alpha$ -Mn-type noncentrosymmetric sample. Upon further increasing the Mo content, in the second superconducting region (for instance at  $x = 0.40$ ), the alloy adopts a  $\beta$ -CrFe-type structure and exhibits a  $T_c = 6.07$  K, relatively lower than that of other phases. The third superconducting region has its onset at  $x \gtrsim 0.5$ , with all the samples showing a bcc-W-type crystal

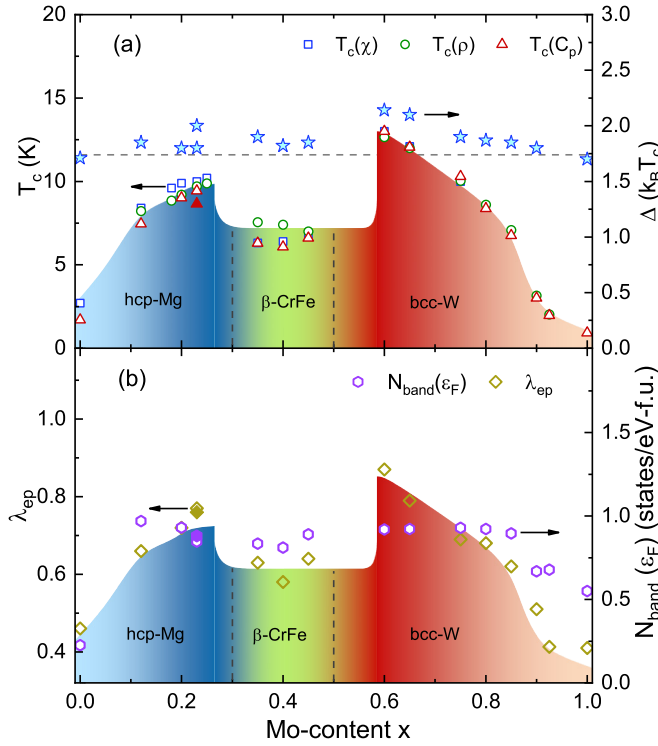


FIG. 7. Superconducting phase diagram of the  $\text{Re}_{1-x}\text{Mo}_x$  alloys. (a) Transition temperatures  $T_c$ , as determined from electrical resistivity, magnetic susceptibility, and specific-heat data, as well as superconducting gap values ( $\star$ , in  $k_B T_c$  units), as determined from fits to the zero-field specific heat vs Mo content. (b) The calculated band-structure density of states  $N_{\text{band}}(\epsilon_F)$  and the electron-phonon coupling constant  $\lambda_{\text{ep}}$  for  $\text{Re}_{1-x}\text{Mo}_x$ . The solid symbols refer to the noncentrosymmetric  $\text{Re}_{0.77}\text{Mo}_{0.23}$  case. Data for  $\text{Re}_{1-x}\text{Mo}_x$  ( $0.8 \leq x \leq 1$ ) were adopted from Ref. [47]. Colors highlight the correlation between SC properties and crystal structure.

structure and the highest  $T_c$  reaching 12.4 K at  $x = 0.60$ . In all the regions, specific-heat data evidence a fully gapped superconducting state with a single gap. Compared with the pure Re and Mo superconductors, as well as with the ideal BCS case (for which  $\Delta_0/k_B T_c = 1.76$ ),  $\text{Re}_{1-x}\text{Mo}_x$  alloys with  $0.12 \leq x \leq 0.75$  exhibit larger superconducting gap values, thus indicating moderately coupled superconducting pairs in the latter.

Figure 7(b) shows the calculated band-structure density of states (DOS)  $N_{\text{band}}(\epsilon_F)$  and the electron-phonon coupling constant  $\lambda_{\text{ep}}$  versus the Re/Mo concentration (see Sec. III D for details). Interestingly, the  $\lambda_{\text{ep}}$  follows closely the superconducting phase diagram shown in Fig. 7(a) and assumes its maximum values in correspondence with the highest  $T_c$  in both the bcc-W and hcp-Mg phases. Compared to the pure Re or Mo cases, the enhanced  $\lambda_{\text{ep}}$  again indicates a moderately coupled superconductivity in  $\text{Re}_{1-x}\text{Mo}_x$  alloys. The enhanced DOS in  $\text{Re}_{1-x}\text{Mo}_x$ , on either the Re- or Mo-rich side, may be ascribed to the filling of unoccupied  $d$  bands by

additional Mo or Re  $d$  electrons. In any case, the different DOS values in  $\text{Re}_{1-x}\text{Mo}_x$  alloys seem closely related to their crystal structures.

Finally, we note that recent  $\mu\text{SR}$  studies on noncentrosymmetric  $\text{ReT}$  alloys indicate that TRS is consistently broken in their superconducting states. Since the TRSB occurrence in  $\text{ReT}$  is independent of the particular transition metal, this points at the key role played by Re. To further confirm such conclusion, Re-containing samples with the same stoichiometry but with different crystal structures are ideal candidates. Considering their rich structural and electronic properties for different Re/Mo concentrations, here we could show that  $\text{Re}_{1-x}\text{Mo}_x$  alloys indeed represent such candidates. For example, for  $x = 0.23$ , samples with either noncentrosymmetric  $\alpha$ -Mn-type or centrosymmetric hcp-Mg-type (the same as pure Re) crystal structures can be prepared. Our results demonstrate an intimate relationship between electronic and crystal structures in  $\text{Re}_{1-x}\text{Mo}_x$  alloys, which puts them forward as excellent systems for studying the interplay among the various symmetries in the superconducting state.

## V. CONCLUSION

To summarize, by combining arc melting and annealing processes, we managed to synthesize  $\text{Re}_{1-x}\text{Mo}_x$  binary alloys in a wide range of solid solutions. XRD patterns are consistent with four different solid phases, including hcp-Mg ( $P6_3/mmc$ ),  $\alpha$ -Mn ( $I\bar{4}3m$ ),  $\beta$ -CrFe ( $P4_2/mnm$ ), and bcc-W ( $Im\bar{3}m$ ), of which  $\alpha$ -Mn and  $\beta$ -CrFe have been among the most difficult to obtain to date. As established by electrical-resistivity, magnetic-susceptibility, and heat-capacity measurements across the full range of solid solutions,  $\text{Re}_{1-x}\text{Mo}_x$  exhibits three superconducting regions, with the highest  $T_c$  reaching 9.43 and 12.4 K in the hcp-Mg and  $\beta$ -CrFe phases, respectively. The low-temperature electronic specific heat evidences a fully gapped superconducting state, whose enhanced gap magnitude and specific-heat discontinuity suggest a moderately strong pairing, the latter being consistent with an enhanced electron-phonon coupling constant  $\lambda_{\text{ep}}$ . The close correlation between  $\lambda_{\text{ep}}$ , DOS, superconductivity, and crystal structure indicates that  $\text{Re}_{1-x}\text{Mo}_x$  alloys represent a very interesting system for studying the effects of structural symmetry on the electronic properties. The superconducting phase diagram reported here paves the way to future microscopic investigations, including the use of local-probe techniques such as NMR and  $\mu\text{SR}$ . Forthcoming zero-field  $\mu\text{SR}$  experiments will be essential to clarify the possible influence of structure on the occurrence of TRSB in the  $\text{Re}_{1-x}\text{Mo}_x$  family.

## ACKNOWLEDGMENTS

The authors thank S. Ghosh, J. Quintanilla, P. Puphal, and I. Eremin for fruitful discussions. This work was supported by the Schweizerische Nationalfonds zur Förderung der Wissenschaftlichen Forschung, SNF (Grant Nos. 200021-169455 and 206021-139082).

- [1] *Non-Centrosymmetric Superconductors*, edited by Bauer E. and M. Sigrist, Lecture Notes in Physics Vol. 847 (Springer Verlag, Berlin, 2012).
- [2] M. Smidman, M. B. Salamon, H. Q. Yuan, and D. F. Agterberg, Superconductivity and spin-orbit coupling in non-centrosymmetric materials: A review, *Rep. Prog. Phys.* **80**, 036501 (2017).
- [3] I. Bonalde, W. Brämer-Escamilla, and E. Bauer, Evidence for Line Nodes in the Superconducting Energy Gap of Noncentrosymmetric CePt<sub>3</sub>Si from Magnetic Penetration Depth Measurements, *Phys. Rev. Lett.* **94**, 207002 (2005).
- [4] H. Mukuda, T. Fujii, T. Ohara, A. Harada, M. Yashima, Y. Kitaoka, Y. Okuda, R. Settai, and Y. Onuki, Enhancement of Superconducting Transition Temperature Due to the Strong Antiferromagnetic Spin Fluctuations in the Noncentrosymmetric Heavy-Fermion Superconductor CeIrSi<sub>3</sub>: A <sup>29</sup>Si NMR Study Under Pressure, *Phys. Rev. Lett.* **100**, 107003 (2008).
- [5] H. Q. Yuan, D. F. Agterberg, N. Hayashi, P. Badica, D. Vandervelde, K. Togano, M. Sigrist, and M. B. Salamon, S-Wave Spin-Triplet Order in Superconductors without Inversion Symmetry: Li<sub>2</sub>Pd<sub>3</sub>B and Li<sub>2</sub>Pt<sub>3</sub>B, *Phys. Rev. Lett.* **97**, 017006 (2006).
- [6] M. Nishiyama, Y. Inada, and G.-q. Zheng, Spin Triplet Superconducting State due to Broken Inversion Symmetry in Li<sub>2</sub>Pt<sub>3</sub>B, *Phys. Rev. Lett.* **98**, 047002 (2007).
- [7] G. M. Pang, M. Smidman, W. B. Jiang, J. K. Bao, Z. F. Weng, Y. F. Wang, L. Jiao, J. L. Zhang, G. H. Cao, and H. Q. Yuan, Evidence for nodal superconductivity in quasi-one-dimensional K<sub>2</sub>Cr<sub>3</sub>As<sub>3</sub>, *Phys. Rev. B* **91**, 220502 (2015).
- [8] D. T. Adroja, A. Bhattacharyya, M. Telling, Yu. Feng, M. Smidman, B. Pan, J. Zhao, A. D. Hillier, F. L. Pratt, and A. M. Strydom, Superconducting ground state of quasi-one-dimensional K<sub>2</sub>Cr<sub>3</sub>As<sub>3</sub> investigated using  $\mu$ SR measurements, *Phys. Rev. B* **92**, 134505 (2015).
- [9] H. Kim, K. Wang, Y. Nakajima, R. Hu, S. Ziemak, P. Syers, L. Wang, H. Hodovanets, J. D. Denlinger, P. M. R. Brydon, D. F. Agterberg, M. A. Tanatar, R. Prozorov, and J. Paglione, Beyond triplet: Unconventional superconductivity in a spin-3/2 topological semimetal, *Sci. Adv.* **4**, eaao4513 (2018).
- [10] J. Chen, L. Jiao, J. L. Zhang, Y. Chen, L. Yang, M. Nicklas, F. Steglich, and H. Q. Yuan, Evidence for two-gap superconductivity in the non-centrosymmetric compound LaNiC<sub>2</sub>, *New J. Phys.* **15**, 053005 (2013).
- [11] S. Kuroiwa, Y. Saura, J. Akimitsu, M. Hiraishi, M. Miyazaki, K. H. Satoh, S. Takeshita, and R. Kadono, Multigap Superconductivity in Sesquicarbides La<sub>2</sub>C<sub>3</sub> and Y<sub>2</sub>C<sub>3</sub>, *Phys. Rev. Lett.* **100**, 097002 (2008).
- [12] J. F. Landaeta, D. Subero, D. Catalá, S. V. Taylor, N. Kimura, R. Settai, Y. Ōnuki, M. Sigrist, and I. Bonalde, Unconventional superconductivity and quantum criticality in the heavy fermions CeIrSi<sub>3</sub> and CeRhSi<sub>3</sub>, *Phys. Rev. B* **97**, 104513 (2018).
- [13] I. Bonalde, R. L. Ribeiro, K. J. Syu, H. H. Sung, and W. H. Lee, Nodal gap structure in the noncentrosymmetric superconductor LaNiC<sub>2</sub> from magnetic-penetration-depth measurements, *New J. Phys.* **13**, 123022 (2011).
- [14] J. F. Landaeta, D. Subero, P. Machado, F. Honda, and I. Bonalde, Unconventional superconductivity and an ambient-pressure magnetic quantum critical point in single-crystal LaNiC<sub>2</sub>, *Phys. Rev. B* **96**, 174515 (2017).
- [15] J. Chen, M. B. Salamon, S. Akutagawa, J. Akimitsu, J. Singleton, J. L. Zhang, L. Jiao, and H. Q. Yuan, Evidence of nodal gap structure in the noncentrosymmetric superconductor Y<sub>2</sub>C<sub>3</sub>, *Phys. Rev. B* **83**, 144529 (2011).
- [16] M. Sato and S. Fujimoto, Topological phases of noncentrosymmetric superconductors: Edge states, Majorana fermions, and non-Abelian statistics, *Phys. Rev. B* **79**, 094504 (2009).
- [17] Y. Tanaka, Y. Mizuno, T. Yokoyama, K. Yada, and M. Sato, Anomalous Andreev Bound State in Noncentrosymmetric Superconductors, *Phys. Rev. Lett.* **105**, 097002 (2010).
- [18] S. Chadov, X. Qi, J. Kübler, G. H. Fecher, C. Felser, and S. C. Zhang, Tunable multifunctional topological insulators in ternary Heusler compounds, *Nat. Mater.* **9**, 541 (2010).
- [19] M. Meinert, Unconventional Superconductivity in YPtBi and Related Topological Semimetals, *Phys. Rev. Lett.* **116**, 137001 (2016).
- [20] Z. X. Sun, M. Enayat, A. Maldonado, C. Lithgow, E. Yelland, D. C. Peets, A. Yaresko, A. P. Schnyder, and P. Wahl, Dirac surface states and nature of superconductivity in noncentrosymmetric BiPd, *Nat. Commun.* **6**, 6633 (2015).
- [21] M. N. Ali, Q. D. Gibson, T. Klimczuk, and R. J. Cava, Non-centrosymmetric superconductor with a bulk three-dimensional Dirac cone gapped by strong spin-orbit coupling, *Phys. Rev. B* **89**, 020505 (2014).
- [22] A. D. Hillier, J. Quintanilla, and R. Cywinski, Evidence for Time-Reversal Symmetry Breaking in the Noncentrosymmetric Superconductor LaNiC<sub>2</sub>, *Phys. Rev. Lett.* **102**, 117007 (2009).
- [23] J. A. T. Barker, D. Singh, A. Thamizhavel, A. D. Hillier, M. R. Lees, G. Balakrishnan, D. McK. Paul, and R. P. Singh, Unconventional Superconductivity in La<sub>7</sub>Ir<sub>3</sub> Revealed by Muon Spin Relaxation: Introducing a New Family of Noncentrosymmetric Superconductor that Breaks Time-Reversal Symmetry, *Phys. Rev. Lett.* **115**, 267001 (2015).
- [24] D. Singh, M. S. Scheurer, A. D. Hillier, and R. P. Singh, Time-reversal-symmetry breaking and unconventional pairing in the noncentrosymmetric superconductor La<sub>7</sub>Rh<sub>3</sub> probed by  $\mu$ SR, *arXiv:1802.01533*.
- [25] R. P. Singh, A. D. Hillier, B. Mazidian, J. Quintanilla, J. F. Annett, D. McK. Paul, G. Balakrishnan, and M. R. Lees, Detection of Time-Reversal Symmetry Breaking in the Noncentrosymmetric Superconductor Re<sub>6</sub>Zr Using Muon-Spin Spectroscopy, *Phys. Rev. Lett.* **112**, 107002 (2014).
- [26] D. Singh, J. A. T. Barker, A. Thamizhavel, D. McK. Paul, A. D. Hillier, and R. P. Singh, Time-reversal symmetry breaking in the noncentrosymmetric superconductor Re<sub>6</sub>Hf: Further evidence for unconventional behavior in the  $\alpha$ -Mn family of materials, *Phys. Rev. B* **96**, 180501 (2017).
- [27] D. Singh, Sajilesh K. P., J. A. T. Barker, D. M. Paul, A. D. Hillier, and R. P. Singh, Time reversal symmetry breaking in noncentrosymmetric superconductor Re<sub>6</sub>Ti, *Phys. Rev. B* **97**, 100505(R) (2018).
- [28] T. Shang, G. M. Pang, C. Baines, W. B. Jiang, W. Xie, A. Wang, M. Medarde, E. Pomjakushina, M. Shi, J. Mesot, H. Q. Yuan, and T. Shiroka, Nodeless superconductivity and time-reversal symmetry breaking in the noncentrosymmetric superconductor Re<sub>24</sub>Ti<sub>5</sub>, *Phys. Rev. B* **97**, 020502 (2018).
- [29] T. Shang, M. Smidman, S. K. Ghosh, C. Baines, L. J. Chang, D. J. Gawryluk, J. A. T. Barker, R. P. Singh, D. McK. Paul, G. Balakrishnan, E. Pomjakushina, M. Shi, M. Medarde, A. D. Hillier, H. Q. Yuan, J. Quintanilla, J. Mesot, and T. Shiroka,



- Time-Reversal Symmetry Breaking in Re-Based Superconductors, *Phys. Rev. Lett.* **121**, 257002 (2018).
- [30] A. A. Aczel, T. J. Williams, T. Goko, J. P. Carlo, W. Yu, Y. J. Uemura, T. Klimczuk, J. D. Thompson, R. J. Cava, and G. M. Luke, Muon spin rotation/relaxation measurements of the noncentrosymmetric superconductor  $\text{Mg}_{10}\text{Ir}_{19}\text{B}_{16}$ , *Phys. Rev. B* **82**, 024520 (2010).
- [31] D. Singh, J. A. T. Barker, A. Thamizhavel, A. D. Hillier, D. McK. Paul, and R. P. Singh, Superconducting properties and  $\mu\text{SR}$  study of the noncentrosymmetric superconductor  $\text{Nb}_{0.5}\text{Os}_{0.5}$ , *J. Phys.: Condens. Matter* **30**, 075601 (2018).
- [32] G. M. Luke, Y. Fudamoto, K. M. Kojima, M. I. Larkin, J. Merrin, B. Nachumi, Y. J. Uemura, Y. Maeno, Z. Q. Mao, Y. Mori, H. Nakamura, and M. Sigrist, Time-reversal symmetry-breaking superconductivity in  $\text{Sr}_2\text{RuO}_4$ , *Nature (London)* **394**, 558 (1998).
- [33] Y. Aoki, A. Tsuchiya, T. Kanayama, S. R. Saha, H. Sugawara, H. Sato, W. Higemoto, A. Koda, K. Ohishi, K. Nishiyama, and R. Kadono, Time-Reversal Symmetry-Breaking Superconductivity in Heavy-Fermion  $\text{PrOs}_4\text{Sb}_{12}$  Detected by Muon-Spin Relaxation, *Phys. Rev. Lett.* **91**, 067003 (2003).
- [34] A. D. Hillier, J. Quintanilla, B. Mazidian, J. F. Annett, and R. Cywinski, Nonunitary Triplet Pairing in the Centrosymmetric Superconductor  $\text{LaNiGa}_2$ , *Phys. Rev. Lett.* **109**, 097001 (2012).
- [35] P. K. Biswas, M. R. Lees, A. D. Hillier, R. I. Smith, W. G. Marshall, and D. McK. Paul, Structure and superconductivity of two different phases of  $\text{Re}_3\text{W}$ , *Phys. Rev. B* **84**, 184529 (2011).
- [36] P. K. Biswas, A. D. Hillier, M. R. Lees, and D. McK. Paul, Comparative study of the centrosymmetric and noncentrosymmetric superconducting phases of  $\text{Re}_3\text{W}$  using muon spin spectroscopy and heat capacity measurements, *Phys. Rev. B* **85**, 134505 (2012).
- [37] T. B. Massalski, H. Okamoto, L. Kacprzak, and P. R. Subramanian, *Binary Alloy Phase Diagrams*, 2nd ed. (ASM International, Materials Park, OH, 1996).
- [38] B. W. Roberts, Survey of superconductive materials and critical evaluation of selected properties, *J. Phys. Chem. Ref. Data* **5**, 581 (1976).
- [39] D. P. Shum, A. Bevolo, J. L. Staudenmann, and E. L. Wolf, Enhanced Superconductivity by Electron Renormalization of a Directly Observed Brout-Visscher Local Phonon: Re in  $\text{Mo}_{1-x}\text{Re}_x$ , *Phys. Rev. Lett.* **57**, 2987 (1986).
- [40] M. Okada, E. Rotenberg, S. D. Kevan, J. Schäfer, B. Ujfalussy, G. M. Stocks, B. Genatempo, E. Bruno, and E. W. Plummer, Evolution of the electronic structure in  $\text{Mo}_{1-x}\text{Re}_x$  alloys, *New J. Phys.* **15**, 093010 (2013).
- [41] T. A. Ignatyeva and A. N. Velikodny, Electronic topological transition in  $\text{Mo}_{1-x}\text{Re}_x$  alloys and its influence on the temperature of the superconducting transition, *Low Temp. Phys.* **30**, 388 (2004).
- [42] S. A. Farzadfar, M. Levesque, M. Phejar, and J.-M. Joubert, Thermodynamic assessment of the molybdenum-rhenium system, *Calphad* **33**, 502 (2009).
- [43] Y. Yang, C. Zhang, S. L. Chen, D. Morgan, and Y. Austin Chang, First-principles calculation aided thermodynamic modeling of the Mo-Re system, *Intermetallics* **18**, 574 (2010), and references therein.
- [44] J. Rodríguez-Carvajal, Recent advances in magnetic structure determination by neutron powder diffraction, *Physica B: Condens. Matter* **192**, 55 (1993).
- [45] A. Naor, N. Eliaz, E. Gileadi, and S. R. Taylor, Properties and applications of rhenium and its alloys, *AMMTIAC Quart.* **5**, 11 (2010).
- [46] R. A. Holmwood and R. Glang, Resistivity and temperature coefficient of pure molybdenum, *J. Chem. Eng. Data* **10**, 162 (1965).
- [47] S. Sundar, L. S. S. Chandra, M. K. Chattopadhyay, S. K. Pandey, D. Venkateshwarlu, R. Rawat, V. Ganesan, and S. B. Roy, Strong electron-phonon coupling and multiband effects in the superconducting  $\beta$ -phase  $\text{Mo}_{1-x}\text{Re}_x$  alloys, *New J. Phys.* **17**, 053003 (2015).
- [48] D. C. Rorer, D. G. Onn, and H. Meyer, Thermodynamic properties of molybdenum in its superconducting and normal state, *Phys. Rev.* **138**, A1661 (1965).
- [49] F. Heiniger, E. Bucher, and J. Muller, Low temperature specific heat of transition metals and alloys, *Phys. Condens. Mater.* **5**, 243 (1966).
- [50] D. R. Smith and P. H. Keesom, Specific heat of rhenium between 0.15 and 4.0 K, *Phys. Rev. B* **1**, 188 (1970).
- [51] S. Sundar, L. S. Sharath Chandra, M. K. Chattopadhyay, and S. B. Roy, Evidence of multiband superconductivity in the  $\beta$ -phase  $\text{Mo}_{1-x}\text{Re}_x$  alloys, *J. Phys.: Condens. Matter* **27**, 045701 (2015).
- [52] C. Kittel, *Introduction to Solid State Physics*, 8th ed. (Wiley, Hoboken, NJ, 2005).
- [53] W. L. McMillan, Transition temperature of strong-coupled superconductors, *Phys. Rev.* **167**, 331 (1968).
- [54] A. B. Karki, Y. M. Xiong, N. Haldolaarachchige, S. Stadler, I. Vekhter, P. W. Adams, D. P. Young, W. A. Phelan, and J. Y. Chan, Physical properties of the noncentrosymmetric superconductor  $\text{Nb}_{0.18}\text{Re}_{0.82}$ , *Phys. Rev. B* **83**, 144525 (2011).
- [55] C. S. Lue, H. F. Liu, C. N. Kuo, P. S. Shih, J. Y. Lin, Y. K. Kuo, M. W. Chu, T. L. Hung, and Y. Y. Chen, Investigation of normal and superconducting states in noncentrosymmetric  $\text{Re}_{24}\text{Ti}_5$ , *Supercond. Sci. Tech.* **26**, 055011 (2013).
- [56] Mojammel A. Khan, A. B. Karki, T. Samanta, D. Browne, S. Stadler, I. Vekhter, Abhishek Pandey, P. W. Adams, D. P. Young, S. Teknowijoyo, K. Cho, R. Prozorov, and D. E. Graf, Complex superconductivity in the noncentrosymmetric compound  $\text{Re}_6\text{Zr}$ , *Phys. Rev. B* **94**, 144515 (2016).
- [57] D. A. Mayoh, J. A. T. Barker, R. P. Singh, G. Balakrishnan, D. McK. Paul, and M. R. Lees, Superconducting properties of the noncentrosymmetric superconductor  $\text{Re}_6\text{Hf}$ , *Phys. Rev. B* **96**, 064521 (2017).
- [58] M. J. Winarski, Electronic structure of non-centrosymmetric superconductors  $\text{Re}_{24}(\text{Nb};\text{Ti})_5$  by *ab initio* calculations, *J. Alloys Compd.* **616**, 1 (2014).
- [59] H. Padamsee, J. E. Neighbor, and C. A. Shiffman, Quasiparticle phenomenology for thermodynamics of strong-coupling superconductor, *J. Low Temp. Phys.* **12**, 387 (1973).
- [60] M. Tinkham, *Introduction to Superconductivity*, 2nd ed. (Dover, Mineola, NY, 1996).
- [61] A. Carrington and F. Manzano, Magnetic penetration depth of  $\text{MgB}_2$ , *Physica C* **385**, 205 (2003).